ResearchGate

See discussions, stats, and author profiles for this publication at: https://www.researchgate.net/publication/319213738

Mg-Ion Battery Electrode: An Organic Solid's Herring Bone Structure Squeezed upon Mg-ion Insertion

Article *in* Journal of the American Chemical Society · August 2017

DOI: 10.1021/jacs.7b06313

CITATIONS
0

READS
123

12 authors, including:

Ismael A. Rodríguez Pérez
Oregon State University
12 PUBLICATIONS **73** CITATIONS
SEE PROFILE

Yifei Yuan
Argonne National Lab-University of Illinois at C…
62 PUBLICATIONS **418** CITATIONS
SEE PROFILE

Xingfeng Wang
Oregon State University
29 PUBLICATIONS **1,031** CITATIONS
SEE PROFILE

Lu Ma
The Ohio State University
42 PUBLICATIONS **563** CITATIONS
SEE PROFILE

Some of the authors of this publication are also working on these related projects:

Metal Organic Responsive Frameworks View project

AgCC Cyclizations View project

All content following this page was uploaded by Xiulei David Ji on 24 August 2017.

The user has requested enhancement of the downloaded file.

JACS
JOURNAL OF THE AMERICAN CHEMICAL SOCIETY

Oregon State OSU UNIVERSITY

Subscriber access provided by Oregon State University

Article

Mg-Ion Battery Electrode: An Organic Solid's Herring Bone Structure Squeezed upon Mg-ion Insertion

Ismael A. Rodríguez-Pérez, Yifei Yuan, Clement Bommier, Xingfeng Wang, Lu Ma, Daniel P Leonard, Michael M Lerner, Rich G. Carter, Tianpin Wu, P. Alex Greaney, Jun Lu, and Xiulei Ji

J. Am. Chem. Soc., **Just Accepted Manuscript** • DOI: 10.1021/jacs.7b06313 • Publication Date (Web): 21 Aug 2017

Downloaded from http://pubs.acs.org on August 24, 2017

Just Accepted

"Just Accepted" manuscripts have been peer-reviewed and accepted for publication. They are posted online prior to technical editing, formatting for publication and author proofing. The American Chemical Society provides "Just Accepted" as a free service to the research community to expedite the dissemination of scientific material as soon as possible after acceptance. "Just Accepted" manuscripts appear in full in PDF format accompanied by an HTML abstract. "Just Accepted" manuscripts have been fully peer reviewed, but should not be considered the official version of record. They are accessible to all readers and citable by the Digital Object Identifier (DOI®). "Just Accepted" is an optional service offered to authors. Therefore, the "Just Accepted" Web site may not include all articles that will be published in the journal. After a manuscript is technically edited and formatted, it will be removed from the "Just Accepted" Web site and published as an ASAP article. Note that technical editing may introduce minor changes to the manuscript text and/or graphics which could affect content, and all legal disclaimers and ethical guidelines that apply to the journal pertain. ACS cannot be held responsible for errors or consequences arising from the use of information contained in these "Just Accepted" manuscripts.

ACS Publications

Journal of the American Chemical Society is published by the American Chemical Society. 1155 Sixteenth Street N.W., Washington, DC 20036
Published by American Chemical Society. Copyright © American Chemical Society. However, no copyright claim is made to original U.S. Government works, or works produced by employees of any Commonwealth realm Crown government in the course of their duties.

Mg-Ion Battery Electrode: An Organic Solid's Herring Bone Structure Squeezed upon Mg-ion Insertion

Ismael A. Rodríguez-Pérez[a], Yifei Yuan[b], Clement Bommier[a], Xingfeng Wang[a], Lu Ma[c], Daniel P. Leonard[a], Michael M. Lerner[a], Rich G. Carter[a], Tianpin Wu[c]*, P. Alex Greaney[d]*, Jun Lu[b]*, and Xiulei Ji[a]*

a. Department of Chemistry, Oregon State University, Corvallis, OR, 97331-4003, United States
b. Chemical Sciences and Engineering Division, Argonne National Laboratory, Lemont, IL, 60439, United States
c. X-ray Science Division, Advanced Photon Sources, Argonne National Laboratory, Lemont, IL, 60439, United States
d Materials Science and Engineering, University of California, Riverside, 900 University Ave. Riverside, CA, 92521, United States

ABSTRACT: We report that crystalline 3,4,9,10-perylenetetracarboxylic dianhydride (PTCDA), an organic solid, is highly amenable to host divalent metal ions, i.e., Mg^{2+} and Ca^{2+}, in aqueous electrolytes, where the van der Waals structure is intrinsically superior in hosting charge-dense ions. We observe that the divalency nature of Mg^{2+} causes unique squeezing deformation of the electrode structure, where it contracts and expands in different crystallographic directions when hosting the inserted Mg-ions. This phenomenon is revealed experimentally by *ex situ* x-ray diffraction and transmission electron microscopy, and is investigated theoretically by first-principles calculations. Interestingly, hosting one Mg^{2+} ion requires the coordination from three PTCDA molecules in adjacent columns of stacked molecules, which rotates the columns, thus reducing the (011) spacing but increasing the (021) spacing. We demonstrate that a PTCDA Mg-ion electrode delivers a reversible capacity of 125 mA h g^{-1}, which may include a minor contribution of hydronium storage, a good rate capability of retaining 75 mA h g^{-1} at 500 mA g^{-1} (or 3.7 C), and stable cycle life. We also report Ca^{2+} storage in PTCDA, where a reversible capacity of over 80 mA h g^{-1} is delivered.

Introduction

Energy storage is indispensable in portable electronics, electrified transportation, and load-leveling for intermittent renewable energies.[1,2] Tremendous need of storage exists in remote communities that do not have an access to the grid and in the metropolitan neighborhoods that would be ideally grid-independent for security and economic reasons. Such applications require modular energy storage technologies, where geographically restricted approaches, such as pumped hydro and compressed air, fail to provide solutions.[3,4] This is the gap that can be filled by electrochemical devices, such as batteries and electrochemical capacitors.[5] Despite their dominance in the power battery market, lithium-ion batteries (LIBs) are ill suited for the grid-level storage role. Lithium is subject to serious commodity-price volatility due to the facts that the abundance of lithium in the Earth's crust is low and the locations of known deposits of lithium make its mining geopolitically challenged.[6–8] One intriguing alternative is to employ Mg^{2+} ion as a charge carrier for energy storage systems beyond lithium.[9–13] Magnesium is the 8th most abundant element in the Earth's crust; being divalent, Mg-ions may facilitate higher volumetric charge capacity;[14–16] Mg is far less prone to forming metallic dendrites, the chief cause of failure in Li-ion (Li-metal) cells.[17] Collectively these advantages have stimulated great interests in rechargeable magnesium-ion batteries (MIBs).[12,14,15] However, to date, there are only a handful electrode materials known to reversibly store Mg-ions, and the best known among them is the Chevrel phase of $Mg_xMo_3S_4$.[9–13,15] The difficulty in hosting Mg^{2+} is rooted in its large charge density, where Mg^{2+} (radius of ~0.72 Å with coordination number (CN) of 6)[18] has a similar size as Li^+ (radius of ~0.76 Å with CN of 6)[18] but is of twice the charge.[14] Thus, compared to monovalent cations, e.g., Li^+, Na^+, and K^+, Mg^{2+} is very 'sticky' when migrating through the crystal structures of ionic compounds due to the strong electrostatic interactions between Mg^{2+} and the packing anions.[9,14,17] One strategy is to employ nanostructured electrode materials, which exhibit large capacity values and stable cycling due to their better structural elasticity.[19-20] Furthermore, progress has been made by using integration-type electrodes in reversible Mg/S and Mg/I_2 batteries.[21,22]

Aromatic molecular solids have raised much attention as reversible electrode materials for various types of batteries by storing alkali metal ions, i.e., Li^+, Na^+, and K^+.[23–34,35] Organic solids represent an attractive approach for electrode materials as they occur with remarkable long-range crystallinity, and they are amenable with structural and chemical tunability.[36–38] Unfortunately, in most prior studies pertaining to organic electrodes, attention has rarely been given to the evolution of their crystal structures upon ion insertion.

In this study, we hypothesize that organic molecular solids assembled by van der Waals force and with a lack of ionicity may facilitate reversible insertion/extraction of charge-dense Mg^{2+} and Ca^{2+} ions due to the much milder guest-ion/host interaction. We demonstrate that 3,4,9,10-perylenetetracarboxylic dianhydride (PTCDA), a red pigment, can store Mg-ions reversibly in an aqueous electrolyte. Most

remarkably, upon deep magnesiation (Mg-ion insertion), the PTCDA crystal structure contracts significantly across the (011) crystal planes, where interlayer distance decreases from 9.46 to 8.55 Å, while expanding the spacing in the (021) and (102) interlayers. First-principles calculations using density functional theory (DFT) show that the unit cell volume of PTCDA crystal increases from 734 to 747 $Å^3$ when hosting one Mg^{2+} per PTCDA molecule.

The simultaneous contraction and expansion of lattice planes originates from the divalency of Mg-ions combined with the non-interleaved molecular packing in the PTCDA crystal. Insertion of Mg-ion results in rotation of the columns of stacked PTCDA. Due to the *pi-pi* stacking, the negative charge from the enolates is delocalized across the stacks, giving rise to three PTCDA molecules being coordinated to one Mg^{2+} ion. PTCDA shows excellent Mg-ion storage properties by exhibiting a high initial reversible capacity of 125 mA h g^{-1}, good rate capability by retaining a capacity of over 70 mA h g^{-1} at 500 mA g^{-1} (ca. 3.7 C when 137 mA g^{-1} is defined as 1C, corresponding to one Mg-ion per PTCDA molecule), and good cycling stability.

Experimental Methods

Material preparation. PTCDA powder (Tokyo Chemical Industry Co. Ltd., > 98.0%) was mixed with carbon black (Super-P) and polyvinylidene fluoride (PVdF) with a 7:2:1 mass ratio. This mixture was then ground in N-methyl-2-pyrrolidinone (NMP) solvent for ~ 30 min and was then casted uniformly onto an aluminum foil current collector and dried at ~120 °C under vacuum for ~ 12 hrs. The loading mass per electrode came out to be ~ 1.7 to 2.0 mg cm^{-2}. Further details and cell preparation procedures can be found in the Supporting Information Experimental Details.

Electrochemical characterization. Galvanostatic charge/discharge tests were performed at current densities of 20, 50, 100, 200, and 500 mA g^{-1}, along with cyclic voltammetry with a three-electrode cell using a VMP3 BioLogic potentiostat at a scan rate of 0.1 mV s^{-1}. Furthermore, to assess long-term reversibility of the electrode material under study, cycling tests were conducted in coin cells by a MACCOR battery tester using a current density of 20 mA g^{-1}.

Structural characterization. X-ray diffraction (XRD) patterns were collected on a Rigaku Ultima IV Diffractometer with Cu Kα radiation (λ = 1.5406) in a scan range of 5 to 35° at a scan rate of 1° min^{-1}. Fourier Transform Infrared (FTIR) spectra were recorded on a Nicolet 6700 spectrometer from Thermo Electron. Transmission electron microscopy (TEM) imaging was done in a JEOL JEM-ARM equipped with a cold field emission gun operated at 200 kV. The electrode materials were scratched from the current collector and immersed in DI water under sonication for several minutes. The sample was then loaded into a TEM grid via drop-casting before imaging. The energy dispersive x-ray spectroscopy (EDX) results were obtained using an Oxford X-max 100TLE windowless SDD X-ray detector incorporated into the same TEM described above.

Computational. Calculations were carried out using generalized gradient approximation (GGA) and the Perdew-Burke-Eznerhof (PBE) functional (GGA-PBE)[39] using a DFT-D3 dispersion correction.[40] PTCDA structural simulations were modeled using a Visualization for Electronic and Structural Analysis (VESTA[41]) software Version 3. Further details can be found in the Supporting Information Calculation Details.

Results and Discussion

Electrochemical Characterization. It is well known that it is difficult to use Mg metal as a counter/reference electrode due to its MgO passivated surface. As our primary purpose is to reveal Mg-ion storage properties of PTCDA, we employed a 'cleaner' model system using a three-electrode cell with an aqueous electrolyte (**Figure S1**). In these cells, Ag/AgCl (in sat. KCl) was used as the reference electrode. A self-standing film of activated carbon with the specific surface area of ~ 2300 m^2 g^{-1} and a uniform pore size distribution around 2 nm served as the counter and positive electrode,[42] the PTCDA electrode was the working and negative electrode, and a saturated $Mg(NO_3)_2$ aqueous solution (4.8 M) was employed as the electrolyte at room temperature. During cell charging, the activated carbon electrode was polarized and attracts anions, forming an electrical double layer, whereas the PTCDA electrode incorporates Mg-ions. We used excessive mass of activated carbon electrode so that it was the PTCDA working electrode that limits the cell's capacity.

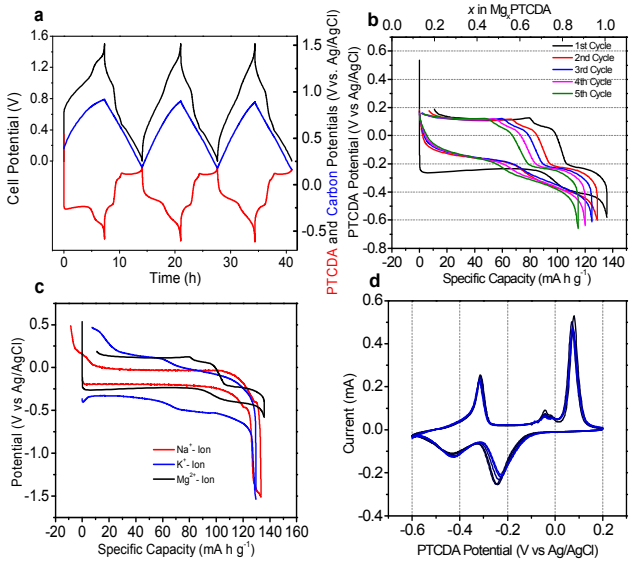

Figure 1. (**a**) The first three cycles of three-electrode cell measurements: full-cell voltage profiles (black) along with profiles of the PTCDA electrode (red) and the activated carbon electrode (blue), respectively, at a current rate of 20 mA g^{-1} in a cell voltage range of 0-1.5 V. (**b**) Galvanostatic magnesiation/demagnesiation potential profiles of the first five cycles of the PTCDA electrode at a current density of 20 mA g^{-1} in a potential range of -0.6 – 0.2 V vs Ag/AgCl reference electrode. **c**, Galvanostatic potential profiles of the first cycles of the PTCDA electrode for storing Na-ions, K-ions, and Mg-ions at current rates of 10 mA g^{-1}, 20 mA g^{-1}, and 20 mA g^{-1}, respective-

ly. (**d**) Typical cyclic voltammetry profiles of the Mg-PTCDA electrode at a scan rate of 0.1 mV s^{-1}.

Figure 1a shows the charge/discharge potential profiles of the full cell (black curves) as well as the individual electrodes of activated carbon (blue) and PTCDA (red) for the first three cycles. It is evident that the 'full' capacity of the PTCDA electrode can be revealed by this cell setup, where the highest polarized potential of the activated carbon electrode is yet to trigger O_2 evolution reaction, and the lowest potential of the PTCDA electrode does not cause H_2 evolution either. **Figure 1b** shows the galvanostatic magnesiation/demagnesiation potential profiles of the PTCDA electrode in the first five cycles at a current density of 20 mA g^{-1}, where PTCDA exhibits a magnesiation capacity of 136 mA h g^{-1} and a demagnesiation capacity of 125 mA h g^{-1} in the first cycle. Such capacity values are suggestive of a two-electron transfer per PTCDA (theoretical capacity: 137 mAh g^{-1}). Note that PTCDA exhibits similar capacity values in the cases of hosting larger sodium-ions and potassium-ions, as revealed in our prior studies in non-aqueous electrolytes (**Figure 1c**).[23,26] This demonstrates that PTCDA exhibits indiscriminate charge storage properties despite the vast disparity of charge density, empowered by its nature of molecular solids. PTCDA displays two sequential plateaus in the magnesiation process but three plateaus in the demagnesiation process, which is confirmed by the cyclic voltammetry (CV) curves with two pairs of anodic/cathodic peaks and a single minor anodic peak (**Figure 1d**). The minor anodic plateau/peak may be related to the extraction of hydronium ions.[43] Note that the potential profile for the first magnesiation is quite different from the following cycles (**Figure 1b**). We attribute this phenomenon to the transition from single-crystalline pristine PTCDA to polycrystalline cycled PTCDA (to be observed by ex situ characterization). As for the first Mg-ion insertion in PTCDA, it appears to be a two-phase phenomenon, featured by the plat potential profile. Upon further cycling, the potential profiles turn sloping, which indicates a higher extent of single-phase redox reactions in a cycled PTCDA phase.

The distinct multi-plateau characteristic is unique compared to the behavior of Na-ion and K-ion storage in the PTCDA electrode when non-aqueous electrolyte is employed. For sodiation/desodiation, PTCDA exhibits a single-plateau behavior, whereas it is a quasi-two-plateau process for K-ion storage (**Figure 1c**). It is evident that the two consecutive reversible redox processes with respect to Mg-ion insertion/extraction are of different degrees of polarization: ~0.1 V for the lower-potential pair and ~0.3 V for the higher-potential pair. Here, it is necessary to discuss the possible function of water and proton regarding Mg-ion insertion into PTCDA. In our recent study of redox behavior of PTCDA in 1 M H_2SO_4 electrolyte, we observed evidence of reversible hydronium intercalation in the PTCDA lattice.[43] Most recently, Wang et al. reported that H^+ is inserted into MnO_2 before Zn^{2+} ions from a weakly acidic $ZnSO_4$+$MnSO_4$ electrolyte.[44] In **Figure S2**, we plotted the potential profiles for both the Mg-ion electrolyte and the H_2SO_4 (1M) electrolyte. The comparison of two systems reveals that the lower-potential plateaus for the Mg-ion system resemble those of the hydronium system in terms of the potentials as well as the extent of polarization—the gap between charge and discharge profiles. Considering the pH value of 3.5 for the sat. $Mg(NO_3)_2$ being a weak Brønsted-Lowry acid, we postulate that hydroniums are inserted into PTCDA from this Mg-ion electrolyte, where it is a minor event due to the low concentration of protons, but it causes the lower-potential plateaus with less polarization. It is reasonable that hydronium storage is of a lower polarization than Mg-ion storage, where the higher charge density of the latter would cause a greater binding energy to the molecules in the crystal solid and consequently a higher insertion potential with a more sluggish intra-electrode diffusion.

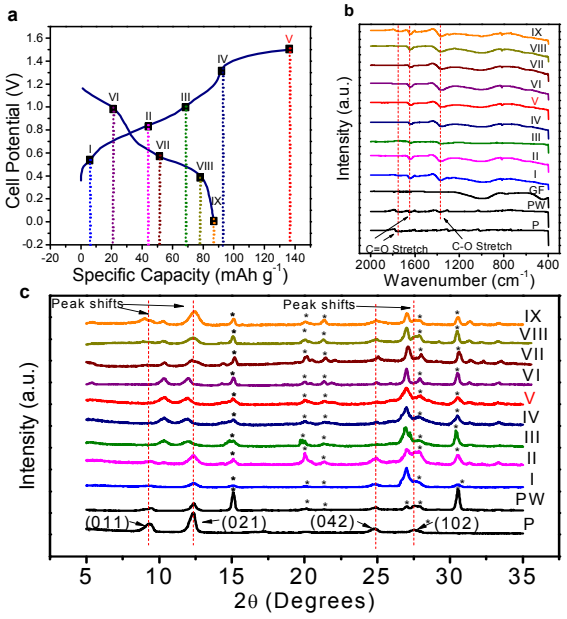

Figure 2. (**a**) Charge/discharge potential profiles of a two-electrode cell, where different SOC is marked. The Roman Numeral V in red represents a fully magnesiated electrode. (**b), (c)** *Ex situ* FT-IR spectra and *ex situ* XRD patterns of PTCDA corresponding to the selected SOC points in (**a**). P stands for the pristine electrode; PW denotes a pristine electrode soaked in the saturated (4.8 M) $Mg(NO_3)_2$ (aq) electrolyte, and GF stands for a glass-fiber separator. A scan of PW was obtained to show that some peaks arose due to the presence of $Mg(NO_3)_2$ residue in the dried electrode; such peaks are indicated by asterisks.

Characterization of Magnesiated PTCDA. The mechanisms of Li-ion or Na-ion storage in carbonyl-containing molecules or polymers are known to be transforming the carbonyl groups to negatively charged enolates.[23,45–47] For the Mg-ion storage in PTCDA, we conducted *ex situ* measurements to characterize the PTCDA electrode at different state of charge (SOC) in two-electrode coin cells, where **Figure 2a** shows the first-cycle charge/discharge potential profiles. The excessive activated carbon still serves as the positive electrode and PTCDA acts as the negative electrode. We confirmed that Mg-ion insertion in PTCDA is also an enolation process, as Li- and Na-ion storage, by FTIR spectra (**Figure 2b**). Upon magnesiation, the carbonyl stretch of the anhydride functional group

at ~1745 cm^{-1} is diminished while a new stretch at ~ 1375 cm^{-1} is strengthened, indicating the conversion from carbonyl groups (C=O) to enolate groups (C-O^-). During demagnesiation, the carbonyl group stretch at ~1745 cm^{-1} recovers; however, the enolate stretch remains, where such irreversibility explains the slightly low first-cycle coulombic efficiency. Furthermore, upon magnesiation, there appears a second carbonyl stretch (C=O) at ~ 1650 cm^{-1}, which is indicative of a carboxylic carbonyl stretch. We believe there exists a certain extent of hydration of the surface regions of the PTCDA electrode particles in the aqueous electrolyte. The hydration of the surface would explain the formation of a second carbonyl stretch (C=O) at ~ 1650 cm^{-1}, which is indicative of a carbonyl stretch without the anhydride functional group. This shows the formation of the perylene tetracarboxylic acid derivative; evidence of surface hydration. Furthermore, the carbonyl stretch at ~ 1650 cm^{-1} persists through the remaining cycling, but the anhydride carbonyl stretch at ~1745 cm^{-1} shows reversible diminishing/re-appearance in concert with (de)magnesiation, indicating that the hydration of PTCDA does not permeate through the whole crystal, and the magnesiation-caused enolation of PTCDA is reversible.

However, to accommodate one Mg^{2+} necessitates enolation of at least two carbonyl groups; this is very different comparing to monovalent Li^+, Na^+, or K^+, where only one carbonyl group binds one cation. Due to the steric limitation, these carbonyl groups cannot possibly come from a single PTCDA molecule, and thus it must be no less than two adjacent PTCDA molecules that coordinate to one Mg^{2+}, which will be further discussed in the computational section below.

To investigate the evolving PTCDA crystal structure upon Mg-ion storage, we collected *ex situ* XRD patterns at different SOC in the first cycle (**Figure 2a,c**). Pristine PTCDA displays a β-form crystal structure that belongs to the monoclinic $P2_1/c$ space group.[23,46] Upon Mg-ion insertion, the most intriguing structural change of PTCDA is the shift of (011) peak to larger 2θ values, where the d-spacing decreases dramatically from 9.46 to 8.55 Å, indicating a severe contraction along one dimension of the PTCDA structure (**Figure 2c**). During the following demagnesiation, the (011) peak is only partially restored, thus suggesting that a portion of the inserted Mg-ions may be trapped in the PTCDA's structure. *Ex situ* EDX results of the "fully" demagnesiated PTCDA confirm the existence of the trapped magnesium (**Figure S3**). *Ex situ* TEM and selected area electron diffraction (SAED) studies also confirm the contraction of PTCDA's structure upon magnesiation (**Figure 3**). The pristine PTCDA electrode consists of sub-micron rods with "clean" morphology and an intact crystalline structure, which is interrupted by magnesiation to be polycrystalline, as shown by the SAED patterns, where the (011) interlayer spacing, indeed, shows contraction (from 10.5 to 9.7 Å) upon magnesiation. Conversely, during the demagnesiation, the (011) d-spacing expands back to 10.5 Å. Notably, the slow capacity decay upon cycling may be attributed to this single-crystalline to polycrystalline transition.

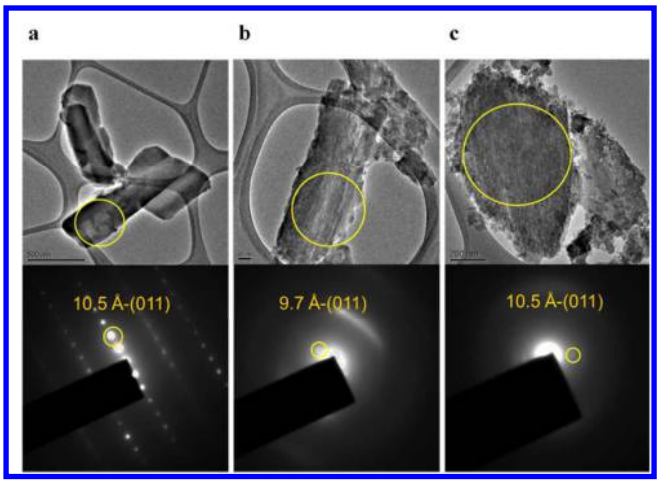

Figure 3. (**a**)-(**c**) *Ex situ* TEM images and SAED patterns of the lateral surfaces of the (011) planes in the (**a**) pristine, (**b**) magnesiated, and (**c**) fully cycled PTCDA electrode (demagnesiated).

Returning to the XRD patterns, the (021) plane shift slightly to lower 2θ angles during magnesiation, which returns to the initial 2θ position upon demagnesiation, thus revealing fully reversible expansion of the (021) planes upon Mg^{2+} insertion/extraction. The situation of the (102) peak (**Figure 4c**) is more complex due to its close proximity to the peaks of residue $Mg(NO_3)_2$. The (102) peak at 27 degrees 2θ increases significantly in intensity, while the peak seems to shift to lower 2θ upon magnesiation. This shift to lower 2θ makes sense, as the Mg^{2+} ions are inserted in between the (102) planes, revealed by computational studies to be discussed (**Figure 4c**). After demagnesiation, the (102) peak is not fully recovered, and the peak at 27 degrees 2θ is still somewhat broader and higher in intensity than in the pristine (electrolyte exposed) PTCDA electrode, suggesting that some Mg^{2+} ions are trapped in the PTCDA structure. Note that in an aqueous system it is a question whether the inserted Mg^{2+} ions are hydrated. Previously, we reported that hydronium ions can be inserted and stored in the same PTCDA electrode,[43] where we observed that multiple XRD peaks of the PTCDA electrode are shifted to lower angles upon hydronium's insertion, indicating quite significant structural expansion (**Figure S4**). We confirmed that such expansion is due to hydronium insertion by density functional theory (DFT) calculations with simulated XRD patterns of hydronium-inserted PTCDA structures (H_3O^+-PTCDA) (**Figure S4**). By comparing the structural change of the PTCDA, particularly the lattice shrinking across the (011) planes, upon Mg-ion insertion and the structural expansion when a hydronium ion is inserted, it is most likely that the inserted charge carrier from the Mg-ion electrolyte represents a smaller size than that of H_3O^+. Furthermore, as a proton is much smaller than a Mg^{2+} ion, the smallest hydrated Mg^{2+}: $Mg^{2+}{\cdot}H_2O$ is likely bulkier than H_3O^+. Along this line, if it were $Mg^{2+}{\cdot}H_2O$ being inserted into PTCDA, a larger scale of lattice expansion than that with H_3O^+ may have taken place. Therefore, we deem that it is most likely the naked Mg^{2+} ions rather than the hydrated forms are inserted into the PTCDA structure.

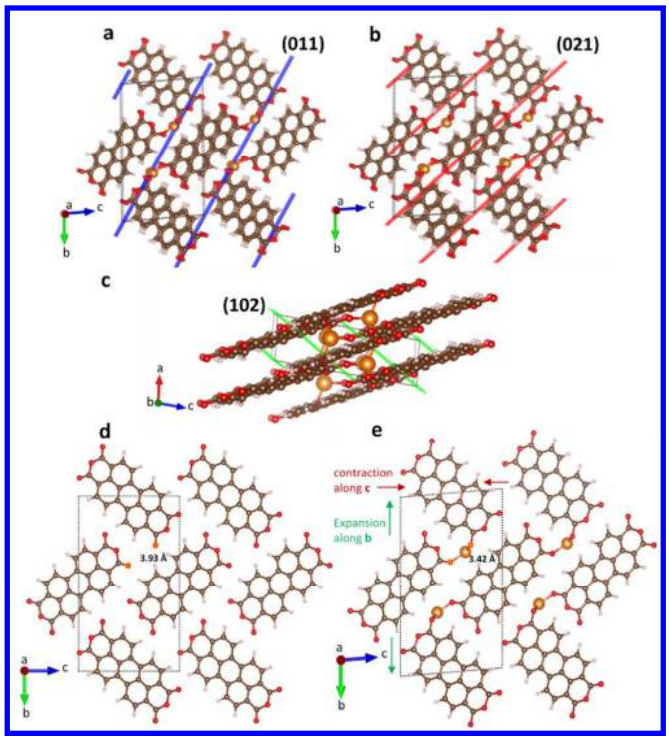

Figure 4. **(a)-(c)** Unit cells in (**a**), (**b**), and (**d**) show the magnesiated PTCDA lattice highlighting the (011), (021), and (102) planes, respectively. (**d)-(e)**, Simulated PTCDA unit cells before (**d**) and after (**e**) magnesiation. The unit cells show a ratio of 1:1 for PTCDA:Mg^{2+}. Unit cells in (**d**) and (**e**) show the distance calculated between two oxygen atoms from two different PTCDA molecules, where their distances are 3.93 Å (pristine) (**d**) and 3.42 Å (with Mg^{2+} inserted) (**e**). The volumes of (**d**) and (**e**) were also calculated to be 734 $Å^3$ and 747 $Å^3$, respectively.

Computational structural calculations. We studied the magnesiation-induced PTCDA contraction by performing first principles calculations to predict the detailed atomic changes in the PTCDA structure under ion insertion. Simulations were also performed with the Mg-ions being located on the basal parts of the PTCDA molecules, as opposed to the holes depicted in **Figure 4a,b**; however, those simulations yield much less favorable formation energies (**Figure S5**), further confirming the assumptions that the Mg-ions occupy the holes. These calculations reveal that the distance between two oxygen atoms that chelate one Mg^{2+} decreases from 3.93 to 3.42 Å from pristine PTCDA to Mg-PTCDA, thus shortening the d-spacing between (011) planes, which are the planes parallel to the columns of stacked PTCDA molecules (**Figure 4a,b,d,e**). Due to the higher electronegativity of oxygen and the added presence of the double bond with the aromatic body of the pristine PTCDA, the edge carbonyl groups are associated with partially negative charges. Thus, these forces cause the PTCDA columns to turn perpendicular to each other, in a 'herring bone' structure, maximizing the distance between carbonyl groups of adjacent molecules, which effectively minimizes the electronic repulsion. Interestingly, the insertion of a positively charged Mg-ion into the structure attenuates the carbonyl/carbonyl repulsion and becomes coordinated by three different carbonyl groups (**Figure 5a**). Although there is evidence of enolation of the carbonyl groups and only two PTCDA molecules would be

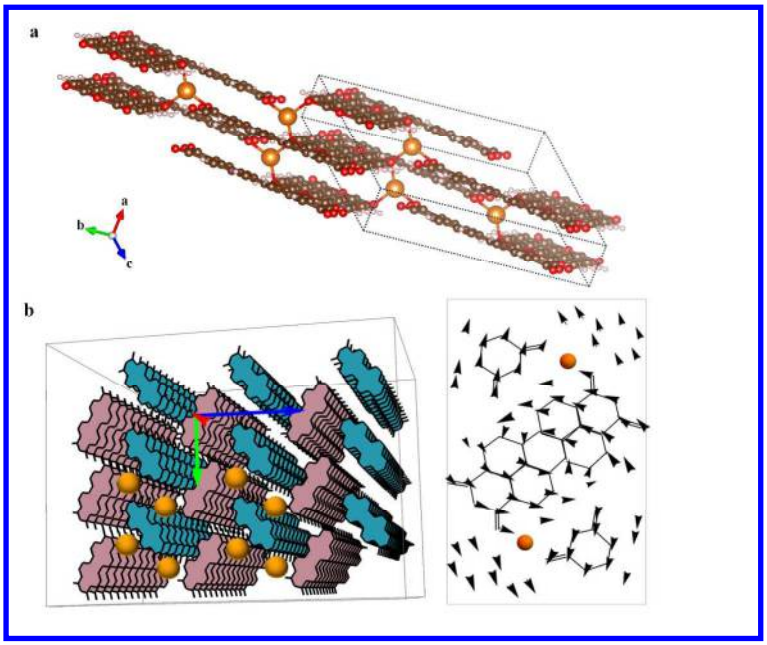

Figure 5. (**a**) Schematic image of the PTCDA crystal lattice showing the coordination of three PTCDA molecules per Mg-ion. (**b**) Schematic image showing the packing of the PTCDA molecules, and how the Mg^{2+} ions sit within the crystal stacks. This shows that the molecules are arranged into independent stacks and the Mg-ions sit in the channels between the coordinated PTCDA molecules in adjacent columns. (**c**) Vector fields showing the mean displacement of atoms upon magnesium insertion, depicting a clear rotation of the individual PTCDA molecules in opposite directions.

expected to chelate to a Mg^{2+} ion, the *pi-pi* stacking nature of the crystal causes the negative charge from the enolates to be delocalized through the stacks, therefore three PTCDA molecules are allowed to coordinate to a single Mg^{2+} ion. As a result of the decreased carbonyl repulsion and the coordination to a Mg^{2+} ion, the PTCDA molecules in the different columns (**Figure 5b**), rotate in separate directions, away from the herring bone arrangement, and towards a more linear arrangement. The rotation of the molecules is clearly seen with in the vector fields (**Figure 5c**), which show the mean displacement that resulted from the insertion of the Mg atoms: individual PTCDA molecules are seen rotating in opposite directions. This rotation of the stacked PTCDA molecules, made possible by the insertion of Mg ions, leads to the slight elongation of the unit cell along the b-axis, but a contraction along the c-axis, explaining the reasons why certain lattice planes contract, such as the (011), while others expand. The *ab initio* structural calculations were performed using density functional theory (DFT) with the Vienna-Ab initio simulation package (VASP). Once the pristine cell parameters were determined (Supporting

Information Calculation Details) a total volume of roughly 758 Å^3 was calculated. The relaxed cell had a volume of approximately 734 Å^3, smaller than the theoretical cell volume. The contraction in the relaxed cell arises from the more efficient packing due to the enhanced 'planar' rearrangement of the relaxed molecules. A suite of calculations was performed to identify the lowest energy binding sites of Mg^{2+} insertion, the details of which are described in the Supporting Information Calculation Details. It is found that the fully relaxed cell containing two inserted Mg atoms (in their ground-state configuration), giving a magnesiation stoichiometry of PTCDA-Mg, possesses an overall volume of about 747 Å^3, thereby confirming the results observed in the *ex situ* XRD and TEM measurements, regarding the overall structural changes. This is in sharp contrast to the cases of insertion 4 Na or 4 K atoms into the PTCDA unit cell, where the new unit cell volumes go up to 805 Å^3 and 863 Å^3, respectively.

Electrochemical rate capability and cycling measurements. We investigated the rate capability of Mg-PTCDA in three-electrode cells. At a high rate of 500 mA g^{-1} or 3.7 C, a capacity of 75 mA h g^{-1} is still retained (**Figure 6a**). This may have to do with its spacious inter-plane space and a lack of ionic bonds in the structure, where ion migration is not impeded. A small increase in polarization is observed upon higher current rates due to the ohmic resistance (**Figure 6b**).

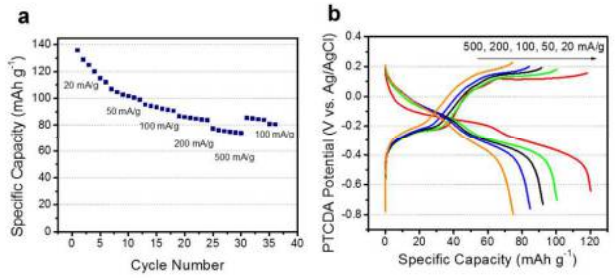

Figure 6 (a) Rate capability measurements at 20, 50, 100, 200, 500, and 200 mA g^{-1}. (**b**) Galvanostatic magnesiation/demagnesiation potential profiles of the PTCDA electrode at different current densities from 20-500 mA g^{-1} in a potential range of -0.8 – 0.4 V vs Ag/AgCl. The profiles shown are from the 4th cycle at each specific current density.

Calcium-ion storage capacity in PTCDA. Inspired by the reversible storage of Mg^{2+} ions, we investigated the electrochemical storage of Ca^{2+} ions in PTCDA. Like magnesium, calcium has significant merit as the working ion in large-scale batteries: it is inexpensive, naturally abundant, chemically safe, and environmentally benign.[48–51] In the early 2000's, vanadium oxides were some of the first electrode materials identified to host Ca^{2+} ions electrochemically.[48,49,52] More recently, however, Prussian blue analogues have attracted much attention for reversible intercalation of Ca^{2+} ions.[51,53,54] Like Mg^{2+} and other multivalent ions, Ca^{2+} is also 'sticky' when migrating through the crystal structures of ionic compounds due to the high electrostatic interactions with a host lattice.[53] We tested galvanostatic charge/discharge performance of a two-electrode cell in coin cells with a self-standing film of activated carbon as the positive electrode and a PTCDA negative electrode in the electrolyte of a saturated $Ca(NO_3)_2$ aqueous solution. An initial capacity of 87 mA h g^{-1} was observed; however, the capacity fades rapidly (**Figure 7a**). The CV curves (**Figure 7b**) show the reversible redox activity of PTCDA with two pairs of anodic/cathodic peaks, indicative of reversible Ca^{2+} ion storage, which is in agreement with the charge/discharge curves.

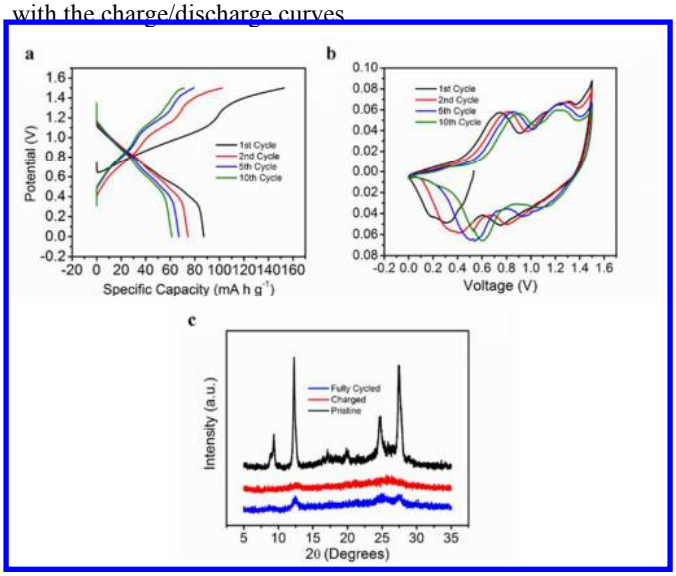

Figure 7. (a) Galvanostatic calciation/decalciation potential profiles of the 1st, 2nd, 5th, and 8th cycles of the PTCDA electrode in a two-electrode cell set-up at a current density of 20 mA g^{-1} in a potential range of 0.0 - 1.5 V. (**b**) Cyclic voltammetry profiles of the 1st, 2nd, 5th, and 10th cycles of the Ca-PTCDA electrode at a scan rate of 0.1 mV s^{-1}. (**c**) *Ex situ* XRD patterns of PTCDA corresponding to the pristine (black), fully charged (red), and a fully cycled (blue) electrode.

XRD patterns of the pristine, calciated electrode, and decalciated electrode reveal the amorphization of the PTCDA crystal when hosting Ca^{2+} ions (**Figure 7c**). The fully calciated electrode shows almost complete amorphization with all XRD peaks gone, although upon full decalciation, some peaks are partially restored. We attribute the amorphization upon cycling to the larger size of the Ca^{2+} ions (radius of ~1.12 Å with CN of 8)[18] as well as the divalency, which bring challenges to the PTCDA host in terms of maintaining its structural integrity.

Conclusions

PTCDA exhibited a reversible Mg-ion storage capacity of 125 mA h g^{-1}, and a good rate capability with 75 mA h g^{-1} at 500 mA g^{-1}. The results reveal that organic solids assembled by van der Waals forces are promising electrodes not only to reversibly host large ions, e.g., Na^+, K^+, but also divalent ions. During magnesiation, the simultaneous contraction and expansion along different crystallographic directions is evident by the characterization of *ex situ* XRD as well as TEM studies, and is confirmed by simulation. Through first-principles calculation, we elucidate that this unique structural change is due

to the divalent nature of Mg^{2+} and the enolation of three PTCDA molecules from neighboring columns of stacked molecules upon coordinating a single Mg^{2+} ion. Finally, we investigated the (de)insertion of Ca^{2+} ions in PTCDA, where a reasonable specific capacity of 80 mA h g^{-1} is demonstrated, and rapid structural amorphization is observed, vastly different from the situation of Mg^{2+}.

ASSOCIATED CONTENT

Supporting Information. Supplementary information is available in the online version of the paper. Reprints and permissions information is available online. This material is available free of charge via the Internet at http://pubs.acs.org.

Experimental details, data and structural simulations.

AUTHOR INFORMATION

Corresponding Authors

*david.ji@oregonstate.edu
*junlu@anl.gov
*agreaney@engr.ucr.edu
*twu@aps.anl.gov

Notes
The authors declare no competing financial interests.

ACKNOWLEDGMENTS

X. Ji is thankful for the financial supports from American Chemical Society Petroleum Research Fund (ACS PRF), Award No. PRF # 55708-DNI10. The use of the Advanced Photon Source, an Office of Science User Facility operated for the U.S. Department of Energy (DOE) Office of Science by Argonne National Laboratory, was supported by the U.S. DOE under Contract No. DE-AC02-06CH11357. We thank OSU EM Facility, funded by National Science Foundation, Murdock Charitable Trust and Oregon Nanoscience and Microtechnologies Institute. This work used the Extreme Science and Engineering Discovery Environment (XSEDE), which is supported by National Science Foundation grant number ACI-1053575. We appreciate the assistance from Professor Douglas A. Keszler on XRD measurements. We also acknowledge Dr. Wei Luo and Dr. Zhenyu Xing for discussion.

REFERENCES

(1) Lu, X.; Xia, G.; Lemmon, J. P.; Yang, Z. *J. Power Sources* **2010**, *195*, 2431–2442.
(2) Ellis, B. L.; Nazar, L. F. *Curr. Opin. Solid State Mater. Sci.* **2012**, *16*, 168–177.
(3) Hittinger, E.; Whitacre, J. F.; Apt, J. *J. Power Sources* **2012**, *206*, 436–449.
(4) Wessells, C. D.; McDowell, M. T.; Peddada, S. V.; Pasta, M.; Huggins, R. A.; Cui, Y. *ACS Nano* **2012**, *6*, 1688–1694.
(5) Conway, B. E. *Electrochemical Supercapacitors: Scientific Fundamentals and Technological Applications*; Springer Science & Business Media: New York, 1999.
(6) Gruber, P. W.; Medina, P. A.; Keoleian, G. A.; Kesler, S. E.; Everson, M. P.; Wallington, T. J. *J. Ind. Ecol.* **2011**, *15*, 760–775.
(7) Miedema, J. H.; Moll, H. C. *Resour. Policy* **2013**, *38*, 204-211.
(8) Mohr, S. H.; Mudd, G.; Giurco, D. *Minerals* **2012**, *2*, 65-84.
(9) Sano, H.; Senoh, H.; Yao, M.; Sakaebe, H.; Kiyobayashi, T. *Chem. Lett.* **2012**, *41*, 1594-1596.
(10) Novák, P.; Imhof, R.; Haas, O. *Electrochim. Acta* **1999**, *45*, 351-367.
(11) Aurbach, D.; Lu, Z.; Schechter, A.; Gofer, Y.; Gizbar, H.; Turgeman, R.; Cohen, Y.; Moshkovich, M.; Levi, E. *Nature* **2000**, *407*, 724-727.
(12) Besenhard, J. O.; Winter, M. *ChemPhysChem* **2002**, *3*, 155-159.
(13) Levi, E.; Gofer, Y.; Aurbach, D. *Chem. Mater.* **2010**, *22*, 860-868.
(14) Yoo, H. D.; Shterenberg, I.; Gofer, Y.; Gershinsky, G.; Pour, N.; Aurbach, D. *Energy Environ. Sci.* **2013**, *6*, 2265-2279.
(15) Yoo, H. D.; Shterenberg, I.; Gofer, Y.; Doe, R. E.; Fischer, C. C.; Ceder, G.; Aurbach, D. *J. Electrochem. Soc.* **2014**, *161*, A410-A415.
(16) Su, S.; Huang, Z.; NuLi, Y.; Tuerxun, F.; Yang, J.; Wang, J. *Chem. Commun.* **2015**, *51*, 2641-2644.
(17) Zhang, R.; Ling, C.; Mizuno, F. *Chem. Commun.* **2015**, *51*, 1487-1490.
(18) Shannon, R. D. *Acta Crystallogr. A* **1976**, *32*, 751-767.
(19) Shao, Y.; Gu, M.; Li, X.; Nie, Z.; Zuo, P.; Li, G.; Liu, T.; Xiao, J.; Cheng, Y.; Wang, C.; Zhang, J.-G.; Liu, J. *Nano Lett.* **2014**, *14*, 255-260.
(20) Cheng, Y.; Shao, Y.; Raju, V.; Ji, X.; Mehdi, B. L.; Han, K. S.; Engelhard, M. H.; Li, G.; Browning, N. D.; Mueller, K. T.; Liu, J. *Adv. Funct. Mater.* **2016**, *26*, 3446-3453.
(21) Gao, T.; Noked, M.; Pearse, A. J.; Gillette, E.; Fan, X.; Zhu, Y.; Luo, C.; Suo, L.; Schroeder, M. A.; Xu, K.; Lee, S. B.; Rubloff, G. W.; Wang, C. *J. Am. Chem. Soc.* **2015**, *137*, 12388-12393.
(22) Tian, H.; Gao, T.; Li, X.; Wang, X.; Luo, C.; Fan, X.; Yang, C.; Suo, L.; Ma, Z.; Han, W.; Wang, C. *Nat. Commun.* **2017**, *8*, ncomms14083.
(23) Luo, W.; Allen, M.; Raju, V.; Ji, X. *Adv. Energy Mater.* **2014**, *4, 1400554*.
(24) Wang, H.; Yuan, S.; Ma, D.; Huang, X.; Meng, F.; Zhang, X. *Adv. Energy Mater.* **2014**, *4, 1301651*.
(25) Wang, H.; Yuan, S.; Si, Z.; Zhang, X. *Energy Environ. Sci.* **2015**, *8*, 3160-3165.
(26) Xing, Z.; Jian, Z.; Luo, W.; Qi, Y.; Bommier, C.; Chong, E. S.; Li, Z.; Hu, L.; Ji, X. *Energy Storage Mater.* **2016**, *2*, 63-68.
(27) Chen, Y.; Luo, W.; Carter, M.; Zhou, L.; Dai, J.; Fu, K.; Lacey, S.; Li, T.; Wan, J.; Han, X.; Bao, Y.; Hu, L. *Nano Energy* **2015**, *18*, 205-211.
(28) Wang, S.; Wang, L.; Zhang, K.; Zhu, Z.; Tao, Z.; Chen, J. *Nano Lett.* **2013**, *13*, 4404-4409.
(29) Wang, S.; Wang, L.; Zhu, Z.; Hu, Z.; Zhao, Q.; Chen, J. *Angew. Chem. Int. Ed.* **2014**, *53*, 5892-5896.
(30) Song, Z.; Qian, Y.; Gordin, M. L.; Tang, D.; Xu, T.; Otani, M.; Zhan, H.; Zhou, H.; Wang, D. *Angew. Chem. Int. Ed.* **2015**, *54*, 13947-13951.
(31) Deng, W.; Shen, Y.; Qian, J.; Cao, Y.; Yang, H. *ACS Appl. Mater. Interfaces* **2015**, *7*, 21095-21099.

(32) Fang, C.; Huang, Y.; Zhang, W.; Han, J.; Deng, Z.; Cao, Y.; Yang, H. *Adv. Energy Mater.* **2016**, *6, 1501727*.
(33) Park, Y.; Shin, D.-S.; Woo, S. H.; Choi, N. S.; Shin, K. H.; Oh, S. M.; Lee, K. T.; Hong, S. Y. *Adv. Mater.* **2012**, *24*, 3562-3567.
(34) Zhao, L.; Zhao, J.; Hu, Y.-S.; Li, H.; Zhou, Z.; Armand, M.; Chen, L. *Adv. Energy Mater.* **2012**, *2*, 962-965.
(35) Wu, X.; Jin, S.; Zhang, Z.; Jiang, L.; Mu, L.; Hu, Y.-S.; Li, H.; Chen, X.; Armand, M.; Chen, L.; Huang, X. *Sci. Adv.* **2015**, *1*,, e1500330-e1500330.
(36) Armand, M.; Grugeon, S.; Vezin, H.; Laruelle, S.; Ribière, P.; Poizot, P.; Tarascon, J.-M. *Nat. Mater.* **2009**, *8*, 120-125.
(37) Walker, W.; Grugeon, S.; Mentre, O.; Laruelle, S.; Tarascon, J.-M.; Wudl, F. *J. Am. Chem. Soc.* **2010**, *132*, 6517-6523.
(38) Liang, Y.; Tao, Z.; Chen, J. *Adv. Energy Mater.* **2012**, *2*, 742-769.
(39) Perdew, J. P.; Burke, K.; Ernzerhof, M. *Phys. Rev. Lett.* **1996**, *77*, 3865-3868.
(40) Moellmann, J.; Grimme, S. *J. Phys. Chem. C* **2014**, *118*, 7615-7621.
(41) Momma, K.; Izumi, F. *J. Appl. Crystallogr.* **2011**, *44*, 1272-1276.
(42) Wang, X.; Chandrabose, R. S.; Chun, S.-E.; Zhang, T.; Evanko, B.; Jian, Z.; Boettcher, S. W.; Stucky, G. D.; Ji, X. *ACS Appl. Mater. Interfaces* **2015**, *7*, 19978-19985.
(43) Wang, X.; Bommier, C.; Jian, Z.; Li, Z.; Chandrabose, R. S.; Rodríguez-Pérez, I. A.; Greaney, P. A.; Ji, X. *Angew. Chem. Int. Ed.* **2017**, *56*, 2909-2913.
(44) Sun, W.; Wang, F.; Hou, S.; Yang, C.; Fan, X.; Ma, Z.; Gao, T.; Han, F.; Hu, R.; Zhu, M.; Wang, C. *J. Am. Chem. Soc.* **2017**, DOI: 10.1021/jacs.7b04471.
(45) Abouimrane, A.; Weng, W.; Eltayeb, H.; Cui, Y.; Niklas, J.; Poluektov, O.; Amine, K. *Energy Environ. Sci.* **2012**, *5*, 9632-9638.
(46) Han, X.; Chang, C.; Yuan, L.; Sun, T.; Sun, J. *Adv. Mater.* **2007**, *19*, 1616-1621.
(47) Novák, P.; Müller, K.; Santhanam, K. S. V.; Haas, O. *Chem. Rev.* **1997**, *97*, 207-282.
(48) Amatucci, G. G.; Badway, F.; Singhal, A.; Beaudoin, B.; Skandan, G.; Bowmer, T.; Plitz, I.; Pereira, N.; Chapman, T.; Jaworski, R. *J. Electrochem. Soc.* **2001**, *148*, A940-A950.
(49) Hayashi, M.; Arai, H.; Ohtsuka, H.; Sakurai, Y. *J. Power Sources* **2003**, *119–121*, 617-620.
(50) Datta, D.; Li, J.; Shenoy, V. B. *ACS Appl. Mater. Interfaces* **2014**, *6*, 1788-1795.
(51) Lipson, A. L.; Pan, B.; Lapidus, S. H.; Liao, C.; Vaughey, J. T.; Ingram, B. J. *Chem. Mater.* **2015**, *27*, 8442-8447.
(52) Hayashi, M.; Arai, H.; Ohtsuka, H.; Sakurai, Y. *Electrochem. Solid-State Lett.* **2004**, *7*, A119-A121.
(53) Padigi, P.; Goncher, G.; Evans, D.; Solanki, R. *J. Power Sources* **2015**, *273*, 460-464.
(54) Wang, R. Y.; Wessells, C. D.; Huggins, R. A.; Cui, Y. *Nano Lett.* **2013**, *13*, 5748-5752.

TOC

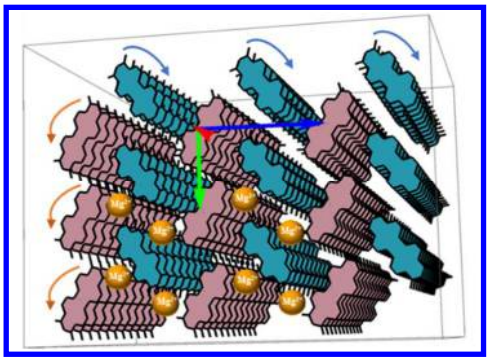

View publication stats